NeuroImage 195 (2019) 203–214

Contents lists available at ScienceDirect

NeuroImage

journal homepage: www.elsevier.com/locate/neuroimage

Mouse BOLD fMRI at ultrahigh field detects somatosensory networks including thalamic nuclei

Won Beom Jung [a,b], Hyun-Ji Shim [a,c], Seong-Gi Kim [a,b,c,*]

[a] Cener for Neuroscience Imaging Research (CNIR), Institute for Basic Science (IBS), Suwon, 16419, Republic of Korea
[b] Department of Biomedical Engineering, Sungkyunkwan University, Suwon, 16419, Republic of Korea
[c] Department of Health Sciences and Technology (SAIHST), Sungkyunkwan University, Seoul, 06351, Republic of Korea

ARTICLE INFO

Keywords:
BOLD fMRI
Mouse
Thalamus
Ketamine
Anesthesia
Ultrahigh fields
Ultrahigh resolution

ABSTRACT

Forepaw somatosensory stimulation induces neural activities in relay thalamic nuclei, the primary somatosensory cortex of forelimb (S1FL), and the secondary somatosensory cortex (S2). However, rodent fMRI studies of somatosensory stimulation have commonly reported BOLD changes only in S1FL, which may be due to side effects of anesthetics and/or the low sensitivity in the thalamus. Thus, we have obtained mouse BOLD fMRI under newly-adopted ketamine-xylazine anesthesia. High-resolution BOLD fMRI obtained with same imaging parameters at 9.4T versus 15.2T shows the improvement of functional detectability by ≥ 2 times at 15.2T due to higher signal intensity and larger BOLD response. The fMRI responses at 15.2T were robustly observed at well-known somatosensory networks including thalamus. Second, echo-time-dependent BOLD signals are dominant based on multi-echo fMRI data. A ratio of BOLD responses in S1FL to thalamus is ~2, which is not related to different baseline T_2^* or different cerebral blood volume. Third, group-averaged 15.2T BOLD maps show activities in S1FL, S2, motor cortices, and thalamic nuclei, which agree well with neural tracing network data from the Allen Institute, demonstrating that fMRI detects entire somatosensory networks. Our data suggest that ultrahigh field fMRI provides a unique window into understanding functional networks in normal and transgenic mouse models noninvasively.

1. Introduction

The mouse is the most widely used animal model in biomedical research due to the abundance of transgenic lines available to study neural circuits and human diseases (Masliah et al., 2000; Vandamme, 2014). Thus, mapping the brain functions of transgenic mice may provide insights into the critical roles of specific genes linked to behavior and disease. This can be achieved noninvasively and repeatedly through the study of blood oxygenation-level dependent (BOLD) functional magnetic resonance imaging (fMRI) in the whole brain (Kim and Ogawa, 2012). Since the utility of fMRI for biomedical research is closely dependent on its ability to accurately detect neural active regions, its detectability has been examined for well-known somatosensory stimulation studies (Brinker et al., 1999; Duong et al., 2000; Hyder et al., 1994; Mandeville et al., 1998; Silva et al., 1999).

Somatosensory stimulation of forepaw induces neural activities in the relay thalamic nuclei, primary somatosensory cortex of forelimb (S1FL), and secondary somatosensory cortex (S2). S1FL has been found to have prominent reciprocal projections with S2, motor cortex and thalamus (Aronoff et al., 2010; Ebner and Kaas, 2015; Petersen, 2014). Although fMRI responses are expected in the entire somatosensory pathway including the thalamus, most anesthetized rat fMRI studies of forepaw stimulation have reported BOLD signal changes only in S1FL (Baltes et al., 2011; Chae et al., 2018; Goloshevsky et al., 2011; Jung et al., 2016; Kim et al., 2010; Komaki et al., 2016; Pelled et al., 2009; Wells et al., 2017; Williams et al., 2010), while only a few fMRI studies showed activities in the thalamus. Thalamic fMRI responses were observed in 5 out of 11 α-chloralose-anesthetized rats at 11.7 T (Keilholz et al., 2004), and were found to be very small in medetomidine anesthetized rats at 9.4 T (Zhao et al., 2008). These inconsistencies may be due to the side effects of anesthetics used for minimizing head motions and stress associated with fMRI scanning, and/or the low BOLD sensitivity in the thalamus.

In mouse fMRI, reliable detection of S1FL activity is not common as well. So far, fMRI studies using the rat-optimized protocol have been attempted to measure reliable BOLD responses in the mouse brain, but most show pain-like widespread brain activities from somatosensory

* Corresponding author. IBS Center for Neuroscience Imaging Research, N Center, Sungkyunkwan University, Suwon, 16419, Republic of Korea.
E-mail address: seonggikim@skku.edu (S.-G. Kim).

https://doi.org/10.1016/j.neuroimage.2019.03.063
Received 17 January 2019; Received in revised form 14 March 2019; Accepted 27 March 2019
Available online 1 April 2019

stimulation (Bosshard et al., 2010; Reimann et al., 2018; Schlegel et al., 2015; Schroeter et al., 2014, 2017). A few mouse fMRI studies at 9.4–11.7 T using medetomidine anesthesia showed the BOLD response localized in the contralateral S1FL, but thalamic response was absent (Adamczak et al., 2010; Nasrallah et al., 2014). In our recent mouse fMRI study with a newly adopted ketamine-xylazine anesthesia at 9.4 T (Shim et al., 2018), we observed robust BOLD response in the contralateral S1FL and weak (but not-significant) response in the contralateral thalamus from forepaw stimulation. Mouse fMRI requires ultrahigh spatial resolution due to the small brain size. Since the response may be dominated by thermal noise-related fluctuations, increasing sensitivity with a higher magnetic field may also increase functional sensitivity (Triantafyllou et al., 2005; Uludag and Blinder, 2018), which may allow us to map somatosensory pathways including the thalamus by fMRI.

In this paper, our aim is to examine whether somatosensory-related brain networks can be mapped in mouse fMRI under ketamine-xylazine anesthesia at an ultrahigh field of 15.2 T. First, to determine field-dependent functional sensitivity, high-resolution BOLD fMRI with $188 \times 188 \times 500\ \mu m^3$ resolution obtained during forepaw somatosensory stimulation at 9.4 T and 15.2 T was compared. Second, echo time (TE)-dependent BOLD responses were measured at 15.2 T to separate TE-dependent and –independent signals. TE-dependent BOLD signals in S1FL and thalamus were compared with relative baseline cerebral blood volume (CBV) to determine the potential source of BOLD signals. Third, group-averaged BOLD maps were compared with neural tracing network data from the Allen Institute (Oh et al., 2014) to examine whether fMRI can indeed detect somatosensory networks.

2. Materials and methods

2.1. Animal preparation and stimulation

Twenty one adult male C57BL/6 mice (23–27 g, 8–14 week old; Orient Bio, Korea) were used with approval by the Institutional Animal Care and Use Committee (IACUC) of Sungkyunkwan University in accordance with the standards for humane animal care. All MRI experiments were performed under anesthesia in accordance with the guidelines of the Animal Welfare Act and the National Institutes of Health Guide for the Care and Use of Laboratory Animals. A mixture of ketamine and xylazine (100 mg/kg and 10 mg/kg, respectively) was initially injected intraperitoneally (IP), and supplementary dose (25 mg/kg ketamine and 1.25 mg/kg xylazine, IP) was intermittently delivered through an IP line based on physiological parameter changes (See details in Shim et al., 2018). The animals were self-breathing under continuous supply of oxygen and air gases (1:4 ratio) through a nose cone at a rate of 1 L/min. To reduce head motions during image scanning, the mouse was carefully positioned on a customized cradle with two ear plugs, a bite bar and a mask. Body temperature was maintained at 37 ± 0.5 °C with a warm-water heating system via rectal temperature probe.

For electrical stimulation, two 30 G needle electrodes were inserted under the plantar skin of the left forepaw, and repeated pulses with a current intensity of 0.3 or 0.5 mA, pulse width of 0.5 ms, and frequency of 4 Hz were applied by a pulse generator (Master 9; World Precision Instruments, Sarasota, FL, USA). These simulation parameters were previously optimized under the same anesthesia (Shim et al., 2018).

2.2. Systemic physiological parameter measurements

Electrocardiogram (ECG) and motion-sensitive respiration signals were continuously measured using a physiological monitoring system (Model 1030, Small Animal Instruments Inc, Stony Brook, USA) and recorded using a data acquisition system (Acknowledge, Biopac Systems, Inc., Goleta, CA, USA). Recorded data were transformed with fast Fourier transformation. Then, the maximum value in the range of 120–360 bpm was selected to obtain heart rates (beats per min) from the ECG and respiration rate (bpm; breath per min) from the motion-sensitive respiration signals. Dynamic pulse and respiration data were averaged over repeated fMRI trials in the same imaging session (see below for fMRI protocol), resulting in averaged dynamic pulse and respiration data in each subject.

2.3. MRI experiments

All MRI experiments were performed on two high field 9.4 T and 15.2 T MR systems (Bruker BioSpec, Billerica, MA, USA); a horizontal bore 9.4 T/30 cm MRI with an actively shielded 12-cm diameter gradient operating with a maximum strength of 66 G/cm and a rise time of 141 μs, and a horizontal bore 15.2 T/11 cm MRI with an actively shielded 6-cm diameter gradient operating with a maximum strength of 100 G/cm and a rise time of 110 μs. A combination of 86 mm inner diameter (ID) volume coil for RF transmission and 10 mm ID surface coil for RF reception was used at 9.4 T, while a 15 mm ID surface coil was used for RF transmission and reception at 15.2 T. The brain was positioned as close to the isocenter of the magnet, and the magnetic field homogeneity was optimized using both global shimming and local shimming on the ellipsoidal volume covering the cerebrum (ParaVision 6, Bruker BioSpin).

Anatomic images with 50 contiguous coronal slices without gap were acquired with the following parameters: field of view (FOV) = $20 \times 20\ mm^2$, matrix = 256×256, in-plane resolution = $78 \times 78\ \mu m^2$, and slice thickness = 300 μm. At 9.4 T, the rapid acquisition with refocused echoes (RARE) sequence was used with repetition time (TR)/TE = 5300/32 ms, RARE factor = 8, and number of excitations (NEX) = 4, while at 15.2 T, the fast low angle shot magnetic resonance imaging (FLASH) sequence was used with TR/TE = 435/2.8 ms, NEX = 5, and flip angle (FA) = 25° (see Supplementary Fig. 1A for one animal's images). These anatomic images were used for the spatial normalization to a common brain space.

Two fMRI studies were performed using gradient echo (GE) echo planar imaging (EPI) with FOV = 18 (readout-out, x-axis) × 12 (phase-encoding, y-axis) mm^2, matrix = 96×64, in-plane resolution = $188 \times 188\ \mu m^2$, slice thickness = 500 μm, contiguous 9 coronal slices without gap, echo time spacing = 320 μs, sampling bandwidth = 300 KHz and dummy scans = 10 (see Supplementary Fig. 1A for one animal's EPI images). To minimize aliasing effects along the phase-encoding dorsoventral direction, a 5-mm-thick section below the brain was saturated before each volume acquisition. Two experimental protocols are described below;

i) Magnetic field-dependent BOLD fMRI at 9.4 T (n = 7) and 15.2 T (n = 7) with the same imaging parameters. Single-shot EPI was used with TR/TE = 1000/16 ms and FA = 60° (9.4 T) and 52° (15.2 T). Stimulation current intensity was 0.5 mA, which was adopted from previous studies (Shim et al., 2018). Each fMRI trial consisted of a 40-s pre-stimulus, 20-s stimulus, and 60-s post-stimulus period.
ii) TE-dependent BOLD fMRI and T_2* measurement at 15.2 T (n = 7). Two-shot EPI was adopted to reduce echo times with parameters of shot-TR/TE = 750/10, 15, and 20 ms. Stimulation current was adjusted to 0.3 mA to minimize ipsilateral S1 activity. Each fMRI trial consisted of a 45-s pre-stimulus, 15-s stimulus, 52.5-s inter-stimulus, 15-s stimulus and 52.5-s post-stimulus period. Three-echo times were acquired in an interleaved manner. To measure relative cerebral blood volume (CBV), baseline T_2^* -weighted images were obtained in all 7 animals using the multi-gradient-recalled echo (Multi-GRE) sequence with the same resolution as functional imaging before and after the intravenous injection of 5 mg/kg iron oxide nanoparticles (Feraheme, AMAG Pharmaceuticals, Waltham, USA). Twenty echoes were acquired with TR/TE = 800/1.5–22.4 ms with an interval of 1.1 ms.

In all fMRI experiments, 10–15 trials were obtained for each condition on each animal with an inter-trial interval longer than 1 min.

2.4. MRI data analysis

Data analyses were performed with the Analysis of Functional Neuroimages package (AFNI) (Cox, 1996), FMRIB Software Library (FSL) (Smith et al., 2004), Advanced Normalization Tools (ANTs) (Avants et al., 2011) and Matlab codes (The Mathworks, Nattick, USA). Twenty echo GRE data were fitted by a mono-exponential function as $S_0 e^{-TE/T_2^*}$, where S_0 is the signal at TE = 0 ms to obtain T_2^* ($1/R_2^*$). Relative baseline CBV was determined by the difference of R_2^* (ΔR_2^*) before and after injection of intravascular susceptibility-induced contrast agent (Kim et al., 2013).

2.4.1. Generation of fMRI maps

Individual animal's BOLD response maps were generated with preprocessing and general linear model (GLM) analysis with a data-driven hemodynamic response function (HRF). The following preprocessing steps were performed to improve the detection of signal activation: slice timing correction, image realignment to each first volume for motion correction, linear detrending for signal drift removal, time course normalization by the average of the baseline volumes, and trial-averaging within the same imaging session. To determine whether the brain motion is synchronized with stimulation, six motion parameters (3 translations and 3 rotations) and frame-wise displacement (FD) were obtained. The FD was calculated by the sum of absolute displacements of the differentiated realignment estimates for each animal (Power et al., 2012). To convert degrees of rotational parameters to millimeters, the mouse brain was assumed as a sphere with a radius of 5 mm (Belloy et al., 2018). Since the statistical value is sensitive to the HRF which is dependent on the anesthetics used (Schlegel et al., 2015), the HRF was determined from the averaged time course of normalized individual subject data in the S1FL region of interest (ROI) (see below for the ROI selection) by fitting with a two-gamma variate function. The two-gamma variate function was chosen for depicting both conventional positive BOLD and post-stimulus BOLD undershoot responses. In individual animal's functional map, the statistically significant activation threshold was set to uncorrected $p < 0.001$ and cluster size > 5 voxels. Individual *t*-value maps were overlaid on original EPI images.

The group-averaged response maps were also generated on the Allen mouse brain space (see Supplementary Fig. 1B). For three TE data obtained from 15.2 T, all three TE data were averaged to enhance the functional detectability before generating group-averaged functional maps. First, the EPI image was co-registered to anatomic image using rigid body transformation. Second, the anatomic image was spatially normalized onto the mouse brain atlas space using both affine and nonlinear transformations. Then, fMRI maps were registered to the mouse brain atlas with the transformation parameters obtained at step #2. The spatial smoothing using a Gaussian kernel with a 0.2 mm full-width at half-maximum (FWHM) was included to minimize the potential misalignment and enhance the statistical power. After GLM analysis, one sample *t*-test was conducted to identify the group-averaged BOLD response, taking into account of a significance at family-wise error corrected $p < 0.05$. The group-averaged fMRI maps were overlaid on the Allen mouse brain atlas (see Supplementary Fig. 1B for processing pipeline).

The group-averaged fMRI maps of the TE-averaged fMRI data were visually compared with the neural connectivity maps from Allen Mouse Brain Connectome Project (http://connectivity.brain-map.org/) in the Allen Institute (Oh et al., 2014). The somatosensory pathways were traced by injecting adeno-associated virus with anterograde presynaptic tracers into the relay ventral group of the dorsal thalamus region (Experiment number 113884251). To compare activation sites in fMRI to projection sites of virus tracing, multiple parameters were determined from fMRI activation clusters; volume, peak *t* value, stereotaxic coordinates and anatomical atlas of the center of mass, and anatomical names within active cluster and their proportion within the cluster. Peak *t* value and stereotaxic coordinates of the center of mass (mm) were calculated from each active cluster. Proportion of functional volume within each active cluster was calculated for each anatomical region. Anatomical regions of virus projection sites were also determined from the connectivity maps and compared with those of fMRI activation sites.

2.4.2. Quantitative analysis

To compare functional sensitivities of images acquired at 9.4 T and 15.2 T, baseline signal-to-noise ratio (SNR) and temporal SNR (tSNR) were calculated from the initial 40 volumes in the pre-stimulus period at a voxel-by-voxel basis. Image noise level was calculated as a standard deviation (SD) of signal intensities measured at four noise ROIs composed of 3D spheres with a radius of 500 μm at each corner of the image, while voxel-wise temporal fluctuation was calculated as SD of 40 pre-stimulus time series data. To assess the relationship between SNR and tSNR, voxel-wise SNR and tSNR within the brain excluding ventricles were correlated and fitted by a linear function. A slope was considered as a linearity value of tSNR to SNR.

For quantitative functional analyses, four different ROIs were selected based on the Allen mouse brain atlas; contralateral S1FL, contralateral thalamus, contralateral S2 and ipsilateral S1FL. ROIs were defined as a 3D sphere with a radius of 500 μm around the center of mass of the activated region from the fMRI map and/or centered on the anatomical location with reference to mouse brain atlas. Several parameters were obtained from the ROIs; i) SNR and tSNR for 9.4 T vs. 15.2 T, ii) baseline T_2* and contrast agent-induced ΔR_2^* for multi-echo data, iii) time course and average *t* value for fMRI studies, and iv) percent changes induced by forepaw stimulation. The percent signal changes over the stimulation duration were averaged excluding the initial 6 s after the stimulus onset to obtain steady-state BOLD responses without the initial transition period. Since the percent signal change can be described as $\Delta S/S_{rest} = -TE \times \Delta R_2^* +$ intercept, the relative contribution of TE-independent intercept and TE-dependent BOLD signals was separated by linear fitting of three TE data as a function of TE.

2.5. Statistical analysis

All quantitative values were represented as mean ± standard error of the mean (SEM). Statistical tests include independent *t*-test for field strength-dependent fMRI and one-way repeated measures analysis of variance (repeated ANOVA) followed by a Bonferroni post-hoc analysis for TE-dependent fMRI. All statistical tests judged significance according to a $p < 0.05$ criterion.

3. Results

3.1. Systemic physiology and motions by somatosensory stimulation

To examine whether systemic vascular physiology and motion are modulated by forepaw stimulation, 180-s-long 15.2 T fMRI runs with two 15-s forepaw stimulus blocks were chosen for demonstration, as opposed to an experimental duration of 120-s fMRI data with one 20-s stimulation. All 7 animal data were averaged in Fig. 1. During experiments (n = 7 animals), the heart rate and the respiratory rate reached 210–240 bpm and 180–200 bpm, respectively, and no noticeable physiological changes were observed by forepaw stimulation (Fig. 1A), which are similar to our previous data (See Fig. 2C in Shim et al., 2018). Motion parameters obtained from image realignment to each first volume (n = 7 animals) are shown in Fig. 1B–D. The maximal translation relative to the first volume was estimated to be 0.0022 ± 0.001 mm along the y-axis direction, corresponding to 1.2% of the voxel dimensions (0.188 mm). This linear displacement in the phase-encoding direction is likely due to slight magnetic field drifts rather than physical movements. The maximal frame-wise displacement was estimated to be 0.0043 ± 0.003 mm which corresponds to 2.3% of the voxel dimension (0.188 mm), indicating that

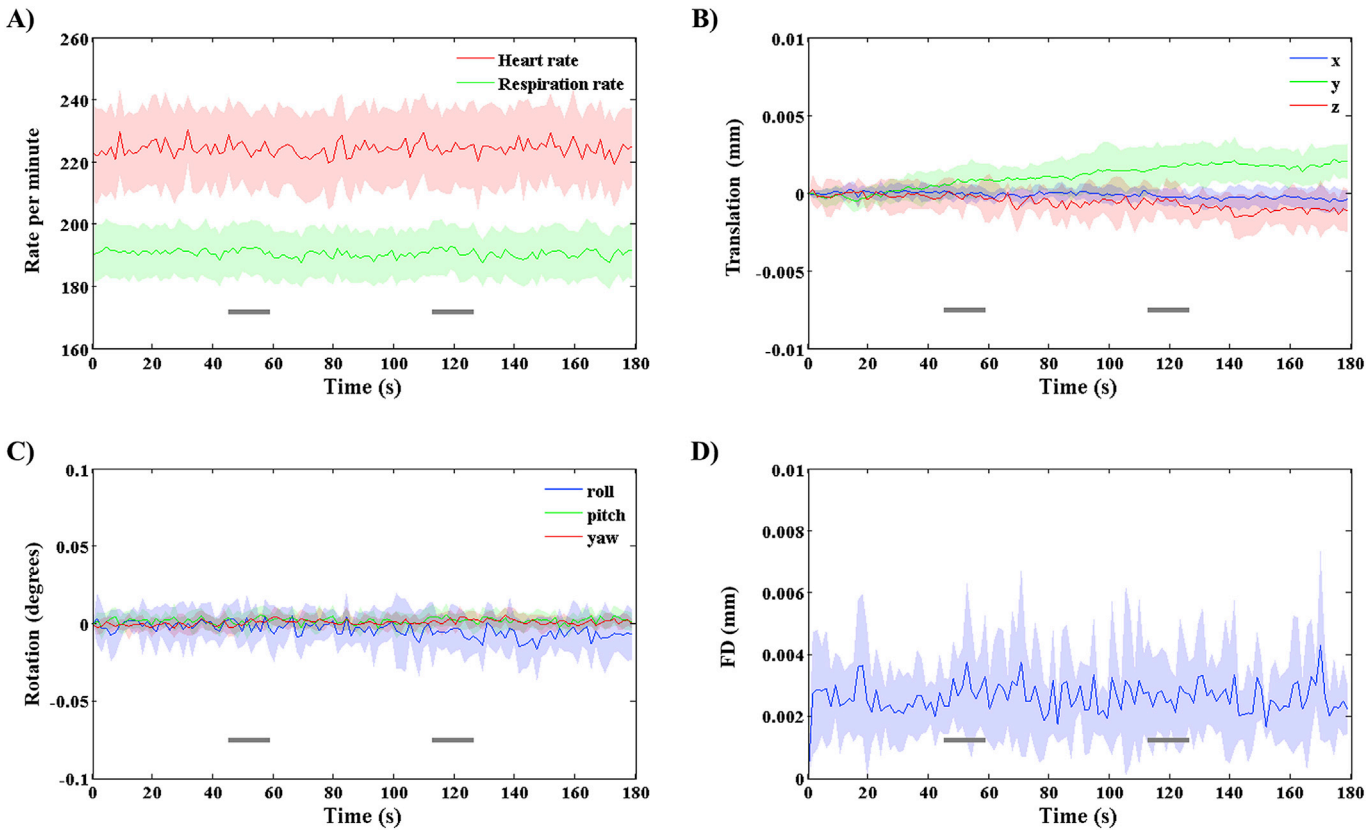

Fig. 1. Physiological parameters and motion parameters acquired during 15.2 T fMRI studies in 7 animals. All data were plotted as mean ± SEM. A) Physiological recordings of heart rate and respiration rate during fMRI experiments. B-C) Translational displacements along the x, y and z direction and rotational displacements of roll, pitch and yaw, relative to the first reference volume. D) Frame-wise displacement (FD) based on the sum of absolute displacements of the differentiated realignment estimates. Rotational displacements were converted from degrees to millimeters with an assumption that the mouse brain is considered as a sphere with a radius of 5 mm. No notable changes were observed in physiological parameters and motion during two 15-s electrical stimulation periods (gray horizontal bars underneath time courses).

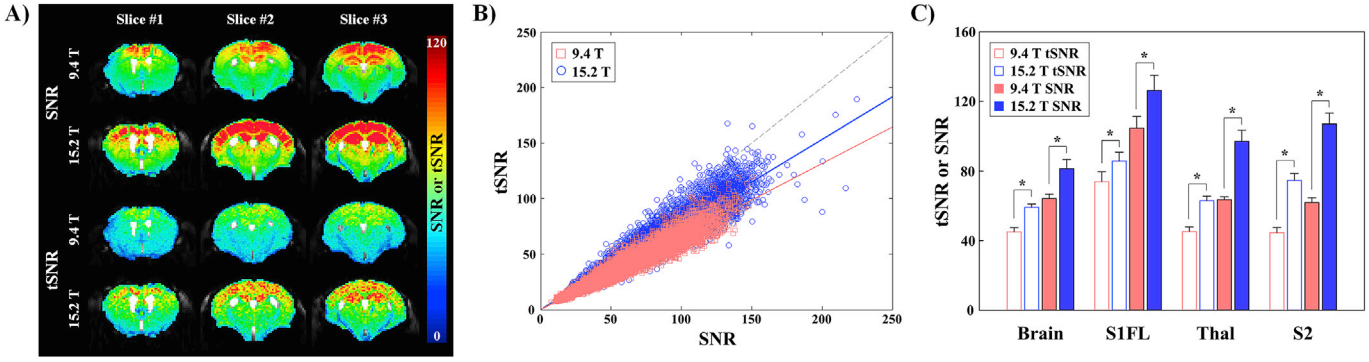

Fig. 2. Field strength-dependent SNR and tSNR in the mouse brain (9.4 T vs. 15.2 T). A) Representative SNR and tSNR maps for one individual animal acquired at 9.4 T and 15.2 T systems. Maps were generated from fMRI data during the pre-stimulus period (40 volumes). Brain SNR and tSNR were measured in the area excluding the ventricle. The remaining 6 animal data at each field strength are shown in Supplementary Fig. 2. B) Temporal SNR (tSNR) as a function of image SNR for all voxels in panel A. The voxels within the brain area from both field strengths are illustrated for 9.4 T (red) and 15.2 T (blue), respectively. The dashed line represents the line of identity (tSNR = SNR), and the solid lines show the linear fit to all voxels. C) Group analysis of tSNR and SNR for the entire brain and three ROIs. The voxel-wise mean SNR and tSNR in each ROI were averaged over seven animals at each field strength. SNR, signal-to-noise ratio; tSNR, temporal SNR; S1FL, forelimb primary somatosensory area; Thal, thalamus; S2, secondary somatosensory area; error bars, SEM; *, $p < 0.05$ (N = 7, respectively, independent *t*-test).

actual motion is minimal and not related to forepaw stimulation (indicated by horizontal bars underneath time courses). Small displacements were corrected by the first volume alignment. Note that nuisance regression approaches including motion parameters, cerebrospinal fluid signals, and signal drift did not improve the detection of task activation (Chuang et al., 2019), suggesting the nuisance removal suitable for human fMRI may not be necessary for anesthetized rodents.

3.2. Magnetic field strength-dependent BOLD fMRI

To compare SNR and functional sensitivity, BOLD fMRI studies induced by forepaw stimulation were performed with the similar

imaging parameters at both magnetic fields. In each subject, average BOLD fMRI trials were 12.4 ± 0.7 at 9.4 T and 12.7 ± 0.8 at 15.2 T. To enhance the sensitivity, all repeated trials in each subject were averaged to produce one averaged time series of volume images in each subject. Voxel-wise SNR and tSNR were calculated from the averaged fMRI runs (Fig. 2, see Suppl. Fig. 2 for SNR and tSNR maps of remaining animals). SNR and tSNR were clearly higher at a higher magnetic field and at the dorsal brain region than the ventral area due to the use of surface coil over the top of the head (see red pixels in Fig. 2A). Voxel-wise tSNR was plotted against SNR for one representative animal at each field (Fig. 2B for data of Fig. 2A). We found that high SNR and tSNR voxels exist more at 15.2 T (see blue circles), and tSNR increases with SNR linearly. Average SNR in the entire brain volume excluding ventricles (Fig. 2C) was 81.4 ± 5.3 at 15.2 T vs. 64.2 ± 2.5 at 9.4 T, and the average tSNR was 59.1 ± 2.0 at 15.2 T vs. 44.9 ± 2.5 at 9.4 T, which is ~70% of SNR. Regional SNR and tSNR values were as follows; in the S1FL ROI, the SNR ratio of 15.2 T/9.4 T is 1.21 (126.3 ± 8.7 vs. 104.6 ± 6.7) and tSNR ratio is 1.16 (85.7 ± 5.1 vs. 73.9 ± 5.7). Note that SNR of single fMRI runs in S1FL was ~35 at 15.2 T and <30 at 9.4 T. In the thalamus region, SNR ratio of 15.2 T/9.4 T is 1.53 (97.1 ± 6.4 vs. 63.5 ± 1.7, $p < 0.001$) and tSNR ratio is 1.39 (63.0 ± 2.6 vs. 45.2 ± 2.6, $p < 0.001$). In S2 region, SNR ratio of 15.2 T/9.4 T is 1.73 (107.1 ± 6.2 vs. 61.9 ± 2.7, $p < 0.001$) and tSNR ratio is 1.67 (74.6 ± 4.0 vs. 44.5 ± 3.0, $p < 0.001$). A ratio of tSNR to SNR is ~0.7, which is independent of a magnetic field strength.

Fig. 3A shows the statistical fMRI maps of one representative animal and group-averaged maps at each magnetic field. To demonstrate the robustness of fMRI maps at 15.2 T, three among 9 slices of the remaining 6 animals were presented in Fig. 4. To show the quality of fMRI data, original EPI images are presented as the underlay for the fMRI maps. High-quality images were obtained with the single-shot GE-EPI sequence even at 15.2 T in all animals (see Fig. 3A–i and Fig. 4).

The HRF which is sensitive to statistical values was determined from actual fMRI time courses of the S1FL ROI (see Supplementary Fig. 3). The two-gamma variate function represents well for both 9.4 T and 15.2 T fMRI data ($R^2 = 0.98$), indicating statistical values can be directly compared between the two magnetic fields. Clearly, the BOLD response at the primary somatosensory area contralateral to the stimulated forepaw was observed with increasing statistical values with increasing magnetic field strength (1st to 3rd column in Fig. 3A). In addition, activities in contralateral thalamus and S2 were reliably detected at 15.2 T (see also 2nd and 3rd row in Fig. 4), but not at 9.4 T (5th and 6th column in Fig. 3A). In order to compare fMRI responses at both fields, fMRI time courses of contralateral S1FL and thalamus ROI were plotted (Fig. 3B and C). The BOLD responses increased during sensory stimulation and post-stimulus BOLD undershoots were detected, which are consistent with findings in our previous 9.4 T mouse fMRI data (Shim et al., 2018). BOLD percent changes also increased with magnetic field strength (3.23 ± 0.17% vs. 1.68 ± 0.08% for contralateral S1FL; 1.60 ± 0.07 vs.

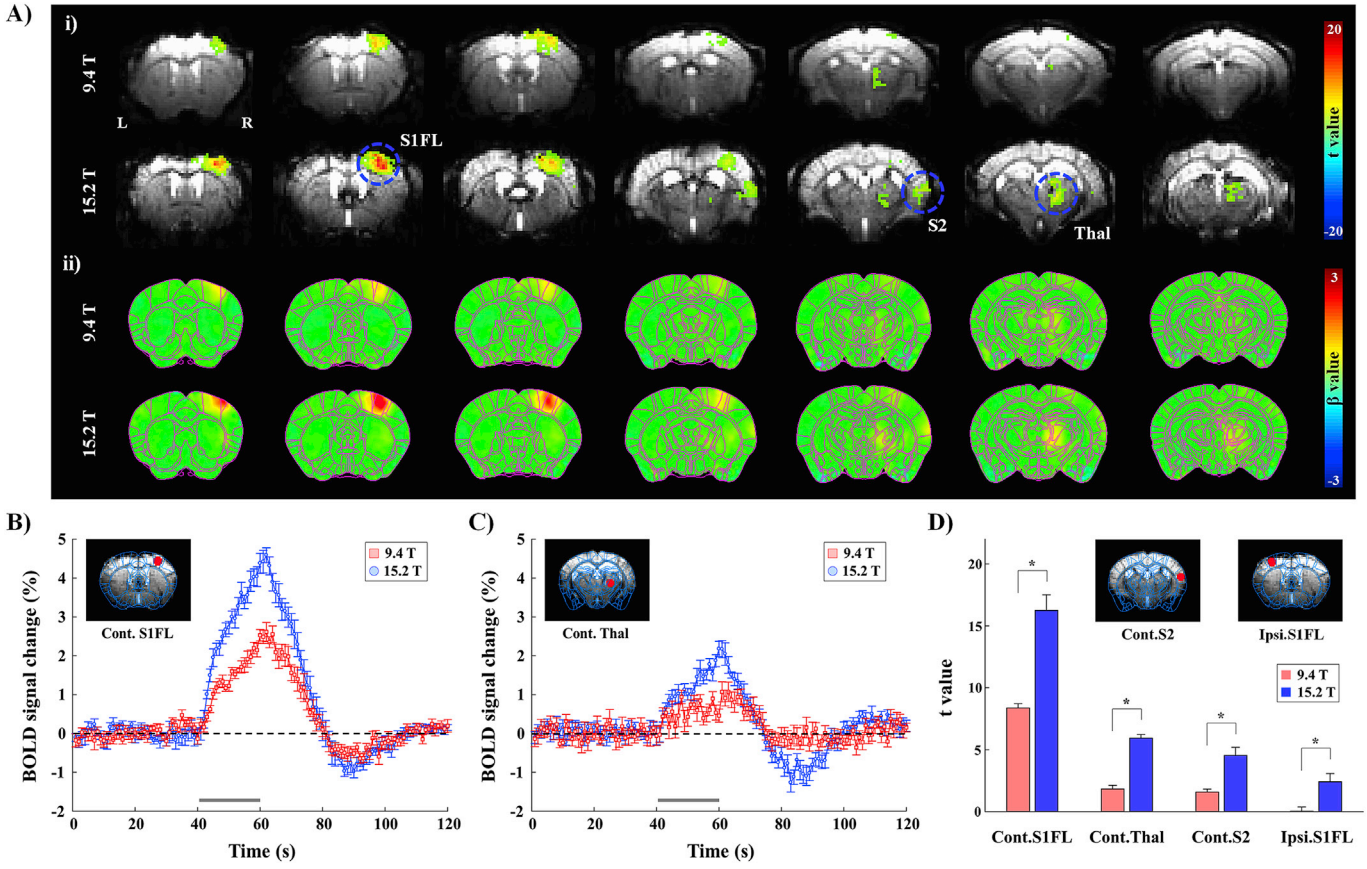

Fig. 3. Field strength-dependent fMRI response to 20-s forepaw stimulation in lightly anesthetized mice (9.4 T vs. 15.2 T). A) Multi-slice fMRI maps of i) one representative animal overlaid on the original EPI image with a statistical threshold (uncorrected $p < 0.001$, cluster size > 5 voxels) and ii) group-averaged analysis without statistical thresholds (N = 7, respectively) at each magnetic field. BOLD fMRI responses were detected in the S1FL, S2 and thalamus at 15.2 T, but in only the S1FL at 9.4 T. The fMRI time courses from the contralateral S1FL (B) and thalamus (C) were obtained from the red ROI in the inset image, respectively, and the average of all seven animals was plotted for 9.4 T (red time courses) and 15.2 T (blue time courses). In each subject, average BOLD fMRI trials were 12.4 ± 0.7 at 9.4 T and 12.7 ± 0.8 at 15.2 T. Error bars, SEM; gray horizontal bar, 20-s stimulus duration. D) Field strength-dependent statistical *t* values from four different ROIs of contralateral S1FL (Cont.S1FL), thalamus (Cont.Thal), S2 (Cont.S2) and ipsilateral S1FL (Ipsi.S1FL). S1FL, forelimb primary somatosensory area; S2, secondary somatosensory area; error bars, SEM; *, $p < 0.05$ (N = 7, independent *t*-test).

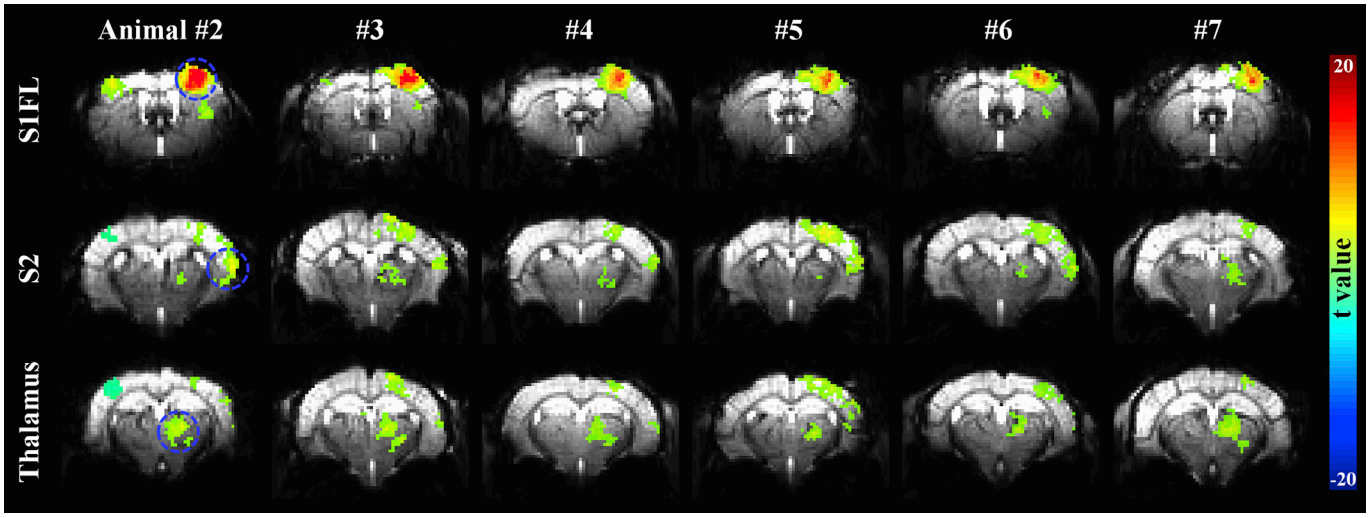

Fig. 4. Evoked fMRI maps of six individual animals obtained at 15.2 T. The statistical threshold was uncorrected $p < 0.001$ and cluster size > 5 voxels. Three slices (rows) containing S1FL, S2 and thalamus were chosen for display, and fMRI maps were overlaid on the original EPI images. Functional activities for 20-s stimulation of the left forepaw were reliably detected in the S1FL, S2 and thalamus at the right hemisphere, except for one mouse (#7) due to signal loss in the lateral boundary of the brain due to the susceptibility effect of ear canals.

$0.58 \pm 0.10\%$ for thalamus; $0.89 \pm 0.13\%$ vs. $0.44 \pm 0.13\%$ for S2; $0.51 \pm 0.07\%$ vs. $-0.05 \pm 0.10\%$ for ipsilateral S1FL).

Average *t* values were calculated within ROIs and compared across the two magnetic fields (Fig. 3D). The statistical *t* value increased at higher magnetic field strength for all calculated regions (16.25 ± 1.26 vs. 8.37 ± 0.35 for contralateral S1FL; 5.94 ± 0.29 vs. 1.83 ± 0.29 for thalamus; 4.55 ± 0.65 vs. 1.59 ± 0.24 for S2; 2.41 ± 0.67 vs. 0.05 ± 0.33 for ipsilateral S1FL). These indicate that functional sensitivity of mouse fMRI increases with magnetic field strength.

Statistically significant ipsilateral S1FL activation was observed in two out of 7 animals (Animal #2 and #3). The average percent signal change in ipsilateral S1FL was $0.51 \pm 0.07\%$ ($N = 7$), which is about 1/6 of the signal change in contralateral S1FL. This weak ipsilateral S1FL fMRI response is somewhat similar to our previous optical imaging data (see Suppl. Fig. 1 in Shim et al., 2018 with 3.3 times weaker CBV response in ipsilateral S1 than contralateral S1), but differs from previous literature having similar bilateral fMRI activations during unilateral paw stimulation (Reimann et al., 2018; Schroeter et al., 2014). Our weak ipsilateral S1FL response is likely due to somatosensory activity via the inter-hemispheric sensory pathway, rather than globally-responding pain processing. In one animal (Animal #2), a peculiar negative fMRI response appeared in the posterior section of the ipsilateral cortex. Careful inspection of its time course indicates spurious artifacts possibly due to quadratic baseline drifts. Thus, the reproducible activity across multiple animals is required for identifying genuine activation sites. Activation in contralateral S1FL, S2 and thalamus regions was consistently observed at 15.2 T across animals.

3.3. TE-dependent BOLD fMRI: source and sensitivity of fMRI

At higher magnetic fields, blood T_1 is increased, leading to higher inflow effects to fMRI signals with short TR. Thus, large fMRI responses observed at 15.2 T may contain significant contributions from non-BOLD effects such as inflow effects. To test this, fMRI data were obtained with TE of 10 ms, 15 ms and 20 ms to investigate the source of fMRI signals. Fig. 5A shows the fMRI maps of three individual TEs and its average overlaid on the original EPI images of one representative animal. At TE of 20 ms, the signal loss was observed in the lateral boundary of the brain due to the susceptibility effect of ear canals. Thus, the functional sensitivity in the secondary somatosensory cortex decreases with TE. Despite no statistical difference between *t* values of different TE values, the highest *t* values within the contralateral S1FL and thalamus ROIs were

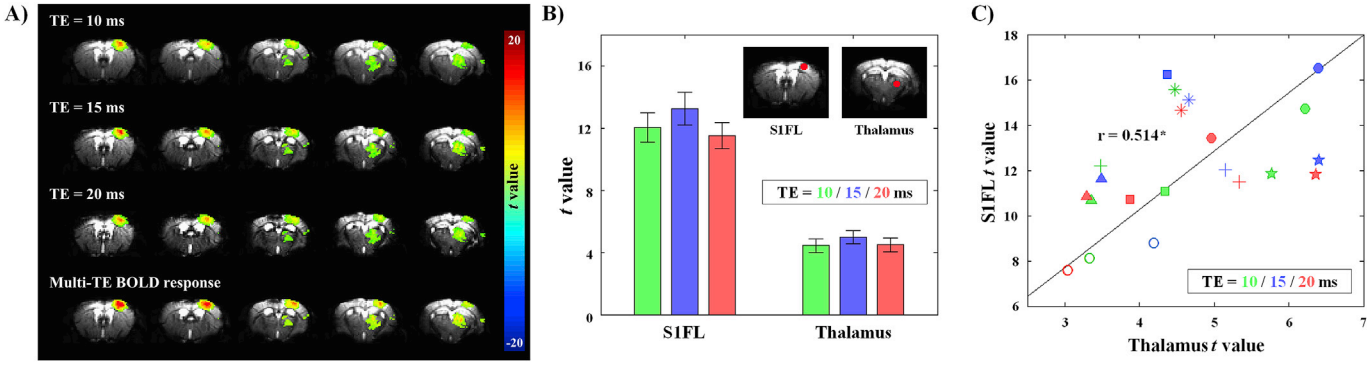

Fig. 5. TE-dependent fMRI at 15.2 T for separating extravascular BOLD and inflow effects. A) Multi-slice fMRI maps overlaid on the original EPI images at multiple-TEs (10 ms, 15 ms, 20 ms and its average) obtained from one individual animal. B) TE-dependence of the statistical *t* value from contralateral S1FL and thalamus ($N = 7$, Mean ± SEM). The *t* values were calculated from the contralateral S1FL and thalamus, depicted as red circles in the inset images. The statistical *t* values in the S1FL and thalamus are the highest at TE of 15 ms, but remain insignificant. C) Twenty one data points in 7 different animals were plotted for determining the relationship between the S1FL and thalamus. Significant linear correlation between the S1FL and thalamus BOLD response was observed. Fitting line, $y = 2.57x$; *, $p < 0.05$ (Pearson correlation).

found to be TE of 15 ms (Fig. 5B), which is similar to baseline T_2^* (14.95 ± 0.64 ms for S1FL and 14.77 ± 0.31 ms for thalamus). Strength of the contralateral S1FL activity is linearly related to that of the contralateral relay thalamus, indicating that the thalamo-cortical interaction can be measured by fMRI (Fig. 5C).

Time courses from the contralateral S1FL and thalamus ROI were obtained (Fig. 6A), and percent changes were plotted as a function of TE (Fig. 6B). Percent signal changes in the contralateral S1FL and thalamus increase with TE (Fig. 6B). The slope of the linearly fitted line of TE-dependent BOLD signals is 89% higher in the contralateral S1FL than in the contralateral thalamus (0.174 vs. 0.092%/ms). Intercepts were close to zero (0.07 and −0.02%), indicating that non-TE-dependent fMRI signal is minimal. Since stimulus-induced ΔR_2^* (-1.74 and −0.92 s^{-1}) is closely dependent on a change in total deoxyhemoglobin contents (e.g., oxygen saturation change × baseline CBV), the difference of functionalΔR_2^* (S1FL/thalamus = 1.89) may simply reflect the difference in baseline CBV.

Relative baseline CBV was determined in the same animals used for fMRI studies. R_2^* was determined from multi-GRE data before and after an intravascular injection of iron oxide nanoparticles (Fig. 6C), and their R_2^* difference is related to relative baseline CBV. Since relative CBV of S1FL and thalamus are similar ($CBV_{S1FL}/CBV_{thal} = 0.92$) (Fig. 6C–ii), the difference in functional ΔR_2^* between S1FL and thalamus is indeed attributed to different changes in oxygen saturation levels.

3.4. BOLD response vs. neural tracing connectivity

To increase the detectability of functional activity, three-TE 15.2 T fMRI data for each animal were averaged to produce one time series of volume images. Group functional maps were calculated and overlaid on a mouse brain atlas (Fig. 7A). The fMRI maps show three functional clusters; contralateral S1FL, contralateral S2 (a lateral activation site of the −1.455 mm slice) and contralateral thalamus. Activation sites of somatosensory and thalamus areas were expanded for better visualization (Fig. 7C). Contralateral dorsal cortical activities include the primary sensory cortex and primary motor cortex (M1). Contralateral thalamic activities centered on the posterior complex of thalamus (PO) include the ventral posterolateral nucleus (VPL) and ventral posteromedial nucleus (VPM). Table 1 tabulates the activated volume, peak *t* value, stereotaxic coordinates of the center of mass, anatomical atlas names of fMRI sites, and its proportion of activation volume within each cluster. The S1FL cluster covers mostly the sensory cortex and motor cortex, while the thalamus cluster centered on the PO includes ventral, lateral and medial nuclei of thalamus.

Our forepaw stimulation-induced fMRI maps (Fig. 7A) were visually compared with the neural connectivity maps obtained from Allen Mouse Brain Connectome Project (http://connectivity.brain-map.org/) (Fig. 7B). The injected tracers in the ventral group of the dorsal thalamus may diffuse into nearby thalamic nuclei including VPL and PO, and the projected tracers were found on various regions including S1FL and S2, M1 and striatum dorsal region. Interestingly, anatomical neural connectivity maps are topologically consistent with the fMRI networks determined by 15.2 T BOLD fMRI (see boldface anatomical names in Table 1).

4. Discussions

We evidently demonstrated our ability to map functional somatosensory networks with BOLD fMRI in lightly anesthetized mice at an ultrahigh field of 15.2 T. The main findings are: 1) an increase in sensi-

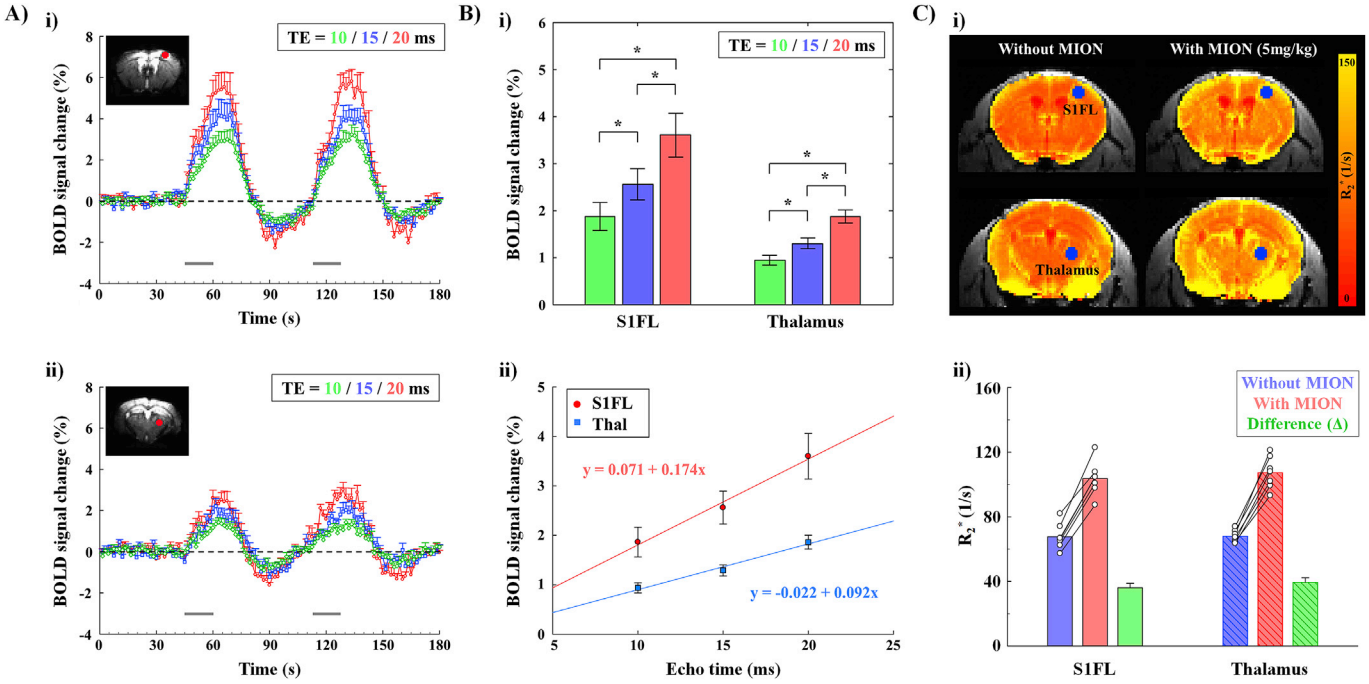

Fig. 6. Determination of sources of fMRI response from TE-dependency and baseline CBV distribution. A) The average of fMRI time courses from the contralateral i) S1FL and ii) thalamus for all animals at TE of 10 ms (green), 15 ms (blue) and 20 ms (red) (N = 7, respectively, Mean ± SEM). 15-s gray bar, stimulus duration. B) TE-dependent percent signal changes from the contralateral S1FL and thalamus. Percent signal changes in the contralateral S1FL and thalamus i) significantly increase with TE (*, $p < 0.05$; repeated ANOVA followed by Bonferroni post hoc test), and ii) show a linear dependency on TE with a close-to-zero intercept. The solid lines are linear fits to the data of the S1FL (red) and thalamus (blue). C) Baseline relative CBV distribution. i) Maps of R_2^* were obtained from multi-GRE data with and without injection of 5 mg/kg MION. The changes in R_2^* induced by iron oxide nanoparticles indicate baseline distribution of total CBV. ii) R_2^* of the SIFL (filled) and thalamus (hashed) before (blue) and after the injection of iron oxide nanoparticles (red), and its difference (green; ΔR_2^*). The ΔR_2^* related to baseline CBV is similar for S1FL and thalamus are (ΔR_2^* ratio = 0.92). Small circles with connected solid lines, individual animal data.

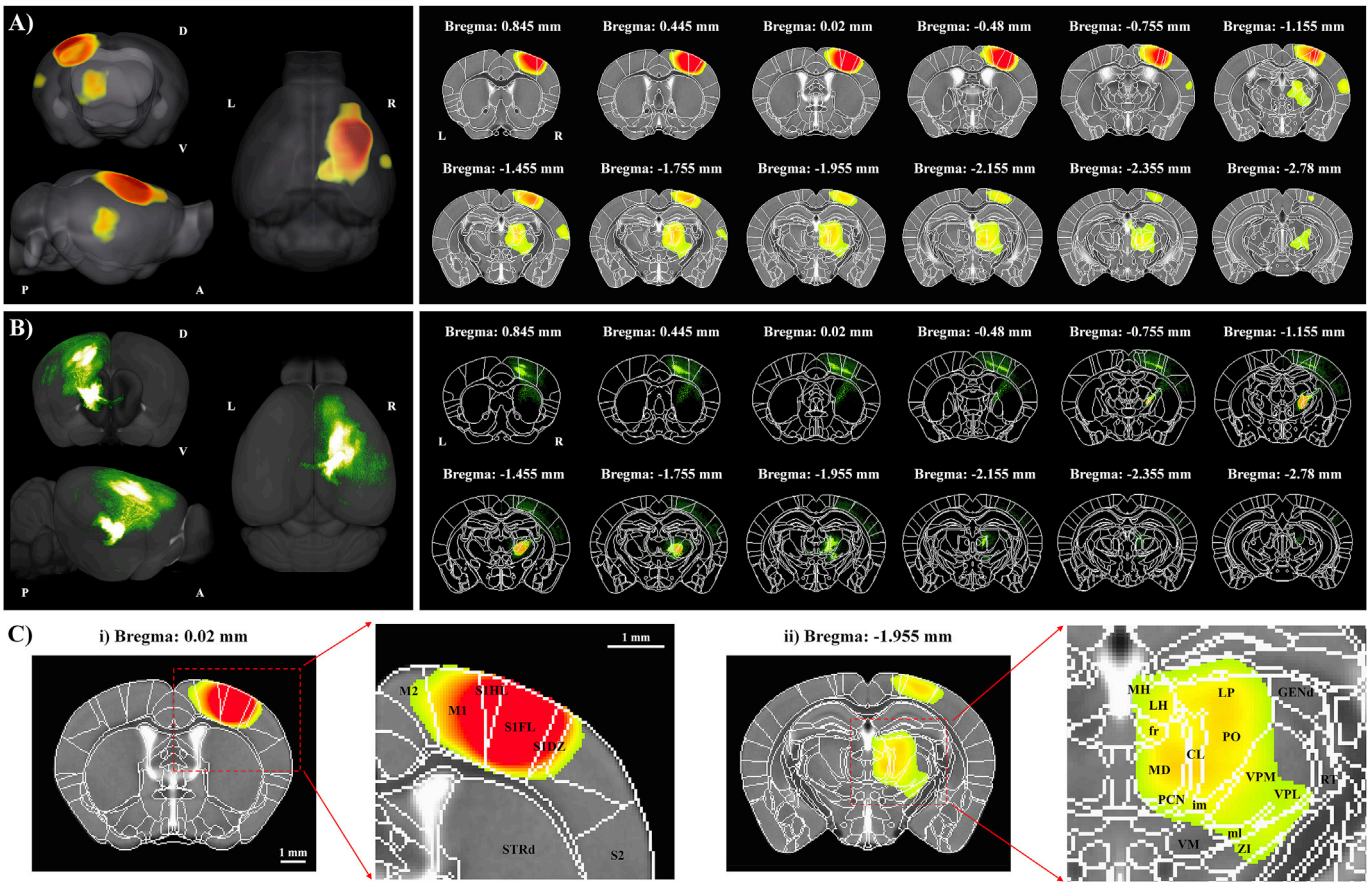

Fig. 7. Group-averaged fMRI vs. neural connectivity maps from the Allen Institute. A) Group-averaged fMRI maps responding to forepaw stimulation (TE-averaged fMRI data, N = 7, FWE corrected $p < 0.05$). The fMRI data were spatially co-registered into Allen mouse brain coordinates. Multiple 2-dimensional slices were arranged from anterior to posterior and its position was indicated as stereotaxic coordinates from the Bregma. The fMRI map shows three functional clusters centered in the S1FL, S2 and thalamus contralateral to stimulated forepaw. B) Neuronal connectivity maps projected from the ventral thalamus, obtained from the Allen Institute (Experimental number 113884251; http://connectivity.brain-map.org/). fMRI sites and virus tracing data are well matched visually. C) A zoomed-in view of fMRI maps of the contralateral S1 and thalamus regions, overlaid on the mouse atlas with labeling. The red dashed box indicates the zoom-in region for the (i) cortex and (ii) thalamus contralateral to the stimulated forepaw. In the cortex, contralateral S1FL and M1 are mainly involved, and the thalamic responses are widespread, including ventral-, lateral- and medial nuclei. D, dorsal; V, ventral; A, anterior; P, posterior; L, left; R, right; S1FL, primary somatosensory area, forelimb; S1HL, primary somatosensory area, hindlimb; S1DZ, primary somatosensory area, dysgranul; S2, secondary somatosensory area; M1, primary motor area; M2, secondary motor area; STRd, striatum, dorsal region; VPL, ventral posterolateral nucleus (of the thalamus); VPM, ventral posteromedial nucleus; VM, ventral medial nucleus; PO, posterior complex; MD, mediodorsal nucleus; CL, central lateral nucleus; LP, lateral posterior nucleus; RT, Reticular nucleus; PCN, paracentral nucleus; GENd, geniculate group, dorsal thalamus; LH, lateral habenula; MH, medial habenula; ZI, Zona incerta; scale bar, 1 mm.

tivity due to higher magnetic field strength improves the functional detectability in the stimulus-related regions, 2) the source of this fMRI response is mostly from the TE-dependent BOLD effects, and the difference in regional BOLD changes are not due to different baseline R_2^* and CBV, 3) the magnitudes of BOLD responses in S1FL and thalamus are correlated and related to different oxygenation level changes, and 4) the macroscopic BOLD fMRI activity sites including the contralateral S1FL, S2 and thalamus are consistent with the neural tracing data obtained from the Allen Institute.

4.1. Use of ketamine and xylazine mixture for mouse fMRI

Various anesthetics have been examined for resting state fMRI and evoked fMRI in mice (Grandjean et al., 2014; Petrinovic et al., 2016; Schroeter et al., 2014). Although a low dose of medetomidine/isoflurane was suggested as a preferred anesthetic due to the existence of bilateral resting state connectivities in cortical and subcortical areas (Grandjean et al., 2014), the tested anesthetics in mice (isoflurane, medetomidine, profopol, urethane, and etomidate) induced non-specific bilateral fMRI responses to somatosensory stimulation in conjunction with stimulation-induced heart rate changes (Petrinovic et al., 2016; Reimann et al., 2018; Schroeter et al., 2014). These indicate that the mouse is still sensitive to pain under light anesthesia. Thus, it is crucial to find an alternative anesthetic for somatosensory fMRI studies.

The combination of ketamine (N-Methyl-D-aspartate receptor antagonist) and xylazine (α2-adrenoceptor agonist) was successfully used for our fMRI studies (Shim et al., 2018). Ketamine is well known as a dissociative anesthetic that antagonizes the N-methyl-D-aspartate (NMDA) receptor (Olney et al., 1999; Orser et al., 1997). The effect of ketamine on CBF and metabolism was investigated by quantitative autoradiographic techniques in rats (Cavazzuti et al., 1987). Compared to awake condition, ketamine (with 100 mg/kg IP dose) increases CBF (awake 165 vs. 214 ml/100 g/min) and glucose metabolism (awake 90 vs. 107 μmo1/100 g/min) in the somatosensory cortex, and slightly decreases CBF (awake 180 vs. 169 ml/100 g/min) and metabolism (awake 91 vs. 82 μmo1/100 g/min) in the ventral posterior thalamus. Compared with 1.1–2.5% isoflurane, ketamine/xylazine (with 87/17 mg/kg and 100/10 mg/kg IP dose) reduces both CBF and glucose metabolism in the rat cortical area by ~30% (Lei et al., 2001; Prando et al., 2019), although glucose metabolism reduction is relatively less in the primary

Table 1
Cluster information of the fMRI maps responding to forepaw stimulation.

Cluster #	Volume (mm^3)	Peak *t* value	Center of Mass (Bregma coords.)				Functional label	
			AP	ML	DV	Annotation	Annotation	Proportion (%)
1	10.84	19.83	−0.16	2.1	1.15	S1FL	Sensory areas (***S1FL***, ***S1HL***, ***S1Tr***, ***S1BF***, ***SSp-un***, ***SSp-m***, ***SSp-n***)	49.9
							Motor areas (***M1***, ***M2***)	39.1
							Posterior parietal association areas (***VISa***, ***VISrl***)	6.1
							Retrosplenial areas (***RSPagl***, ***RSPd***)	2.8
							Visual areas (***VISam***, VISpm, VISp)	2.1
2	3.82	6.23	−1.96	1.2	3.45	PO	Ventral group (***VPM***, ***VAL***, ***VPL***, ***VM***, VPMpc, VPLpc)	27.2
							Lateral group (***PO***, ***LP***, POL, SGN)	26.4
							Medial group (***MD***)	10.5
							Intralaminar nuclei (***PF***, ***CL***, ***PCN***)	10.1
							Hypothalamic lateral zone (LZ, ***ZI***)	9.2
							Anterior group (***LD***, AV)	8.1
							Epithalamus (LH, MH)	3.7
							Fiber tracts (fr, ml, ***em***)	2.7
							Subparafascicular nucleus (SPFp)	1.4
							Reticular nucleus (***RT***)	0.7
3	0.66	4.94	−1.16	−4.55	3.05	S2	Sensory areas (***S2***)	89.7
							Auditory areas (AUDv)	4.9
							Visceral areas (VISC)	3.7
							Temporal association areas (TEa)	1.7

The group averaged-response maps show three functional clusters; contralateral S1FL, contralateral thalamus, and contralateral S2 (see Fig. 7). Each cluster extent is expressed as the volumes exceeding the statistical threshold (N = 7, FWE corrected $p < 0.05$). Peak *t* values and stereotaxic coordinates of the center of mass for active clusters (mm) were calculated with corresponding anatomical annotations. The proportion of functional activity within each active cluster was calculated for each annotated anatomy. The regions marked in boldface symbols indicate the activated regions overlapped with the neural tracing response from the Allen Institute (Experiment number 113884251). AP, anterior to posterior; ML, medial to lateral; DV, dorsal to ventral.

somatosensory cortex (Prando et al., 2019). Ketamine slightly reduces the evoked potential by sensory stimulation compared with awake animals (Hayton et al., 1999; Maxwell et al., 2006), and the somatosensory evoked potentials (SEP) were relatively well-maintained after administration of ketamine (Franceschini et al., 2010). In our studies, robust localized fMRI responses are consistently observed without inducing any cardiac and respiratory rate changes, indicating ketamine/xylazine mixture as a viable anesthetic for mouse fMRI.

4.2. Magnetic field strength-dependent functional response

The functional detectability is determined by baseline tSNR and stimulus-induced signal change. The temporal SNR is determined by the MR signal divided by the standard deviation of temporal fluctuations (S/SD). Temporal fluctuations are modulated by both thermal noises (related to sampling rate and coil performance) and physiological fluctuations (related to respiratory and cardiac pulsations) (Kruger and Glover, 2001). Physiological noises are closely dependent on cardiac and respiratory motions, which may be larger in mice than humans due to higher cardiac and respiratory rates and larger blood flow, and can be reduced by synchronizing EPI data acquisitions relative to mechanical ventilation or by post-processing. When the physiological noise is dominant (e.g., SNR > 200 in humans), both SNR and physiological noises modulate together. At SNR less than 100 in humans, tSNR increases with SNR (Bodurka et al., 2007; Triantafyllou et al., 2005), which is related to magnetic field strength, imaging parameters, coil sensitivity, and voxel volume (Kruger et al., 2001; Triantafyllou et al., 2011). Assuming that human findings can be translatable to mouse studies, our observation of 15.2 T vs. 9.4 T data can be explained as below. In our averaged data of 12–13 trials obtained with the same imaging parameters (TE = 16 ms and 188 × 188 × 500 μm^3) except the flip angle, SNR (tSNR) at 15.2 T and 9.4 T was 85 (61) and 65 (46) in the entire brain volume, and 126 (86) and 105 (74) in the S1FL, respectively. Note that SNR and tSNR of averaged data increase by (# of averages)$^{1/2}$. Although SNR is expected to increase with field strength as B_0 to $B_0^{1.65}$ (Pohmann et al., 2016; Uludag and Blinder, 2018), our SNR gain is less than expected mostly due to shorter T_2^* at 15.2 T (17 ms at 15.2 T vs. 27 ms at 9.4 T in the rat S1FL) (Han et al., 2019). When the ratio of physiological to random noise is ~0.9 in humans, tSNR/SNR is reported to be ~0.75 (Triantafyllou et al., 2005), which is similar to our data of ~0.7, indicating that the physiological noise is similar to the random noise level.

The functional detectability is often described as a contrast-to-noise ratio (CNR), which is functional percent signal change (ΔS/S) times tSNR (S/SD) when the random noise is dominant. Compared to 9.4 T, 15.2 T increases GE-BOLD signals in the S1FL ROI by a range of 50%–90% (6.6 vs. 4.3% at TE = 15 ms in Han et al., 2019; 3.2 vs. 1.7% at TE = 16 ms in this study), and tSNR by 16%. Consequently it is expected that CNR increases 70%–120% by using 15.2 T relative to 9.4 T. In the S1Fl area, the average CNR value was 2.77 and 1.24 for 15.2 T and 9.4 T, respectively, which corresponds to our experimental *t*-value ratio in the S1FL ROI (16 vs. 8).

Unlike our observation, CNR was not improved at higher magnetic fields in two other previous field-dependent rat fMRI studies (Han et al., 2019; Seehafer et al., 2010). The major difference between ours and previous studies is voxel resolution; 188 × 188 × 500 μm^3 in the current study, 469 × 469 × 1000 μm^3 for 9.4 T vs. 15.2 T studies (Han et al., 2019), and 400 × 400 × 2000 μm^3 for 7 T vs. 11.7 T studies (Seehafer et al., 2010). Since SNR linearly increases with voxel volume, SNR in previous studies is 12–18 times higher than that of our current study. When our high-resolution 15.2 T data directly translate into low resolution SNR, SNR in the S1FL ROI at 15.2 T is expected to be volume ratio × (126)/(12 averages)$^{1/2}$ and would be 420 in previous 469 × 469 × 1000 μm^3 studies. Consequently, fMRI detectability does not improve because physiological fluctuations and functional changes increase together for low resolution fMRI studies. These are consistent with theoretical expectations (see Fig. 1 in Uludag and Blinder, 2018), in which CNR increases with field strength only for a random-noise dominant case.

In our field-dependent fMRI studies, the same TE of 16 ms was used for both magnetic fields. Functional sensitivity will be the highest when TE = T_2^*. In our studies, the TE set for 15.2 T maximizes fMRI signal (baseline T_2^* = 17 ms at 15.2 T vs. ~27 ms at 9.4 T, Han et al., 2019), thus the measured functional sensitivity at 9.4 T is not maximal. However, Han et al. demonstrated that the functional sensitivity acquired at the optimal tissue TE (30 ms) at 9.4 T increased only 6% compared to that obtained at 15 ms. Therefore, our field-dependent fMRI sensitivity gain is still valid.

SNR at 15.2 T increased by 21% in the S1FL, but 53% in the thalamus

compared to 9.4 T. This differential gain in SNR is likely due to the use of different diameter RF coil (10 mm at 9.4 T vs. 15 mm at 15.2 T). The larger coil used at 15.2 T penetrates deeper, which enhances SNR in the thalamus region. Therefore, the functional detectability in the thalamus and S2 was improved by using a higher magnetic field and a larger diameter coil. Taken together, ultrahigh fields increase the BOLD sensitivity for high-resolution fMRI.

4.3. Signal source of fMRI responses in S1FL and thalamus at 15.2T

The measured fMRI signals have originated from i) extravascular BOLD, ii) intravascular BOLD, and iii) inflow effects (Kim and Ogawa, 2012). Since blood T_2 at 15.2 T is 2–3 ms (Duong et al., 2003; Han et al., 2019), the intravascular BOLD signal is negligible when TE $\geq$ 10 ms. Separation between extravascular BOLD and inflow components can be achieved by multi-TE fMRI. The extravascular BOLD percent change is linearly dependent on TE, while the inflow effect is independent of TE. Since TE-independent intercepts are close to zero, the inflow effect is minimal for our experimental condition.

The forepaw stimulation-induced ΔR_2^* is $-1.74\ s^{-1}$ in S1FL and $-0.92\ s^{-1}$ in the thalamus, which can be approximately described as $-\Delta S_{o2} \times CBV_v + \Delta CBV_v \times S_{o2}$ where S_{o2} is the venous oxygenation level and CBV_v is the venous cerebral blood volume (Kim and Ogawa, 2012). During 20-s forepaw stimulation, venous CBV change is expected to be negligible (Kim et al., 2007). Therefore, ΔR_2^* is directly related to a change in venous oxygenation level weighted by baseline venous CBV. Since baseline CBV measured by the contrast agent was similar for S1FL and thalamus, the difference in functional ΔR_2^* between S1FL and thalamus is indeed attributed to different ΔS_{o2}.

4.4. Thalamic fMRI response in response to somatosensory stimulation

One of our major findings is that the functional responses were reliably detected in the contralateral thalamus during forepaw stimulation at 15.2 T. The thalamus is well known as the gate that transmits sensory nerve signals to the cortex. Ventral posterior (VP) and posterior (PO) thalamic relay nuclei have reciprocal connections with S1. In addition, the corticothalamic activity modulates inhibitory gamma aminobutyric acid (GABA)-ergic neurons in the thalamic reticular nucleus (TRN) (Guillery and Harting, 2003; Krause et al., 2003), which in turn projects strongly to the thalamic relay nuclei, including VP and PO. Consequently, the recurrent thalamic activity is closely dependent on direct excitatory corticothalamic and inhibitory TRN activities (Sherman, 2016).

Unlike reproducible well-localized activation in the primary somatosensory cortex, fMRI responses in thalamic nuclei have not been observed well in numerous rodent studies. Only a few fMRI studies showed activities in thalamus in response to somatosensory stimulation. Keilholz et al. performed spin-echo BOLD fMRI of forepaw stimulation under α-chloralose at 11.7 T (Keilholz et al., 2004) and found thalamic activities of 6.4% in 5 out of 11 animals studied. Zhao et al. reported thalamic responses of 0.5% (GE fMRI at TE = 15 ms) under medetomidine at 9.4 T (Zhao et al., 2008). Inconsistent detection of thalamus fMRI response during somatosensory stimulation is possibly due to poor fMRI sensitivity and/or weak thalamic neural activity under anesthesia. In previous somatosensory studies of rodents, 4–10% BOLD response is often observed in the primary somatosensory cortex at 9.4–11.7 T (Han et al., 2019; Nair and Duong, 2004; Pelled et al., 2009; Silva and Koretsky, 2002). If our S1FL/thalamus fMRI ratio of ~2 is applied, then BOLD response of 2–5% is expected in the thalamus, which can be easily detected at high fields. Since the strong S1 response is observed, the thalamocortical activity is likely to be intact. However, the corticothalamic activity may be decreased by the reduction of pyramidal neuronal outputs from layer 6. Furthermore, conventional GABAergic agonistic anesthetics (such as isoflurane) may activate TRN and reduce thalamic activities further causing the resultant hemodynamic response to be quite weak, which is not readily detectable by fMRI.

Our consistent observation of the thalamic fMRI response at 15.2 T can be explained partly by the use of ketamine anesthesia. Ketamine is well known as a NMDA receptor antagonist (Olney et al., 1999; Orser et al., 1997). At sub-anesthetic dose, ketamine is widely utilized to investigate the mechanisms underlying the schizophrenia-like psychosis or antidepressant behaviors in both human and rodent (Maeng et al., 2008; Seamans, 2008; Vollenweider and Kometer, 2010). These studies suggested that 1) ketamine inhibits the NMDA receptors on GABAergic interneurons, thereby disinhibiting firing of glutamatergic pyramidal neurons, and 2) the subsequent increase in glutamate levels leads to an increased activation of α-amino-3-hydroxy-5-methyl-4-isoxazole propionic acid (AMPA) receptors relative to NMDA receptors in the functional circuits. Thus, corticothalamic glutamatergic activity is expected to increase under ketamine anesthesia. The effect of NMDA antagonist on GABAergic interneurons in TRN reduces inhibitory inputs to thalamic relay nuclei. Combination of increased direct corticothalamic excitatory and decreased inhibitory inputs under ketamine anesthesia may increase thalamic activities, which induce detectable BOLD fMRI signals in the thalamus at ultrahigh fields. Further systematic studies are necessary for investigating the strength of thalamic activities under lightly anesthetized conditions.

4.5. Detection of stimulus-related functional circuits by BOLD signal

The forelimb sensory information is transmitted to the specialized somatosensory nuclei in the thalamus, VPL and PO, via the spinal cord and hindbrain (Francis et al., 2008; Paxinos, 2014). Note that commonly-investigated VPM receives inputs from the whiskers. These recipient thalamic nuclei in turn project to layer 4 of primary and secondary somatosensory cortices and is subsequently processed within local synaptically connected neocortical microcircuits across layers (Herkenham, 1980; Liao and Yen, 2008; Lopez-Bendito and Molnar, 2003; Nicolelis and Fanselow, 2002). Reciprocal corticocortical projections are found between S1 and S2, and between S1 and M1. The excitatory pyramidal neurons of S1 and S2 send long-range glutamatergic projections to VPL, VPM and PO thalamic nuclei (Brett-Green et al., 2004; Choi et al., 2016; Ebner and Kaas, 2015; Liao et al., 2010). Primary somatosensory cortex also projects to striatum, thalamic reticular nucleus, and zona incerta (Aronoff et al., 2010; Jones, 2012; Wilson, 2014; Zakiewicz et al., 2014).

In our 15.2 T fMRI studies, BOLD responses in S1, S2, M1, and thalamus were observed in individual animals and group-averaged maps, which is the first time to demonstrate fMRI of the somatosensory networks in rodents to our best knowledge. The fMRI activation in S1, S2 and M1 matched well with the expected circuits and the Allen Institute virus tracing from ventral thalamus. In subcortical areas, activation in the thalamic region was broadly distributed in sensory-related thalamic relay nuclei of VPL, VPM, and PO, and non-sensory-related thalamic nuclei including mediodorsal nucleus (MD). Widespread BOLD responses in the thalamus beyond the known somatosensory circuits may be due to the following methodological and physiological reasons. 1) Since gradient-echo BOLD fMRI is sensitive to draining venous vessels, activation sites spread along draining vessels and also by poor spatial specificity (Zhao et al., 2006). 2) Limited spatial resolution, spatial smoothing during data processing (0.2 mm FWHM) and animal-wise group averaging blur activation foci. 3) Corticothalamic projections from active motor cortical areas may contribute to fMRI responses significantly, spreading fMRI responses in the thalamus. Further systematic studies are necessary to examine sources of widespread thalamic activities.

5. Conclusions

The present study showed that an increase in magnetic field strength improves temporal SNR and detectability of stimulus-induced signal change. Due to the increased BOLD sensitivity at 15.2 T, fMRI responses

were observed on the entire somatosensory networks including the thalamic nuclei during forepaw stimulation in lightly anesthetized mouse, which are consistent with conventional network tracing virus studies. This suggests that ultrahigh-field mouse fMRI opens a new research avenue to measure functional circuits in the whole brain non-invasively, allowing investigations of functional development, recovery, and reorganization in normal and transgenic models.

Acknowledgements

We thank Dr. Yun Bok Kim, Dr. Han Sol Lee and Mr. Andrew You for scientific discussions on data, Dr. Kyoung-Nam Kim and Mr. Han Joong Kim at Gachon University for RF coil design and Mr. Chanhee Lee for maintaining the MR instruments.

Appendix A. Supplementary data

Supplementary data to this article can be found online at https://doi.org/10.1016/j.neuroimage.2019.03.063.

Funding

This project is funded by the Institute for Basic Science in Korea (IBS-R015-D1).

References

Adamczak, J.M., et al., 2010. High field BOLD response to forepaw stimulation in the mouse. Neuroimage 51, 704–712.
Aronoff, R., et al., 2010. Long-range connectivity of mouse primary somatosensory barrel cortex. Eur. J. Neurosci. 31, 2221–2233.
Avants, B.B., et al., 2011. A reproducible evaluation of ANTs similarity metric performance in brain image registration. Neuroimage 54, 2033–2044.
Baltes, C., et al., 2011. Increased blood oxygen level-dependent (BOLD) sensitivity in the mouse somatosensory cortex during electrical forepaw stimulation using a cryogenic radiofrequency probe. NMR Biomed. 24, 439–446.
Belloy, M.E., et al., 2018. Dynamic resting state fMRI analysis in mice reveals a set of Quasi-Periodic Patterns and illustrates their relationship with the global signal. Neuroimage 180, 463–484.
Bodurka, J., et al., 2007. Mapping the MRI voxel volume in which thermal noise matches physiological noise–implications for fMRI. Neuroimage 34, 542–549.
Bosshard, S.C., et al., 2010. Assessment of brain responses to innocuous and noxious electrical forepaw stimulation in mice using BOLD fMRI. Pain 151, 655–663.
Brett-Green, B., et al., 2004. Two distinct regions of secondary somatosensory cortex in the rat: topographical organization and multisensory responses. J. Neurophysiol. 91, 1327–1336.
Brinker, G., et al., 1999. Simultaneous recording of evoked potentials and T2*-weighted MR images during somatosensory stimulation of rat. Magn. Reson. Med. 41, 469–473.
Cavazzuti, M., et al., 1987. Ketamine effects on local cerebral blood flow and metabolism in the rat. J. Cereb. Blood Flow Metab. 7, 806–811.
Chae, S.Y., et al., 2018. Physical exercise enhances adult cortical plasticity in a neonatal rat model of hypoxic-ischemic injury: evidence from BOLD-fMRI and electrophysiological recordings. Neuroimage 188, 335–346.
Choi, J.S., et al., 2016. Eliciting naturalistic cortical responses with a sensory prosthesis via optimized microstimulation. J. Neural Eng. 13, 056007.
Chuang, K.H., et al., 2019. Evaluation of nuisance removal for functional MRI of rodent brain. Neuroimage 188, 694–709.
Cox, R.W., 1996. AFNI: software for analysis and visualization of functional magnetic resonance neuroimages. Comput. Biomed. Res. 29, 162–173.
Duong, T.Q., et al., 2000. Functional MRI of calcium-dependent synaptic activity: cross correlation with CBF and BOLD measurements. Magn. Reson. Med. 43, 383–392.
Duong, T.Q., et al., 2003. Microvascular BOLD contribution at 4 and 7 T in the human brain: gradient-echo and spin-echo fMRI with suppression of blood effects. Magn. Reson. Med. 49, 1019–1027.
Ebner, F.F., Kaas, J.H., 2015. Chapter 24 - somatosensory system. In: Paxinos, G. (Ed.), The Rat Nervous System, fourth ed. Academic Press, San Diego, pp. 675–701.
Franceschini, M.A., et al., 2010. The effect of different anesthetics on neurovascular coupling. Neuroimage 51, 1367–1377.
Francis, J.T., et al., 2008. Proprioceptive and cutaneous representations in the rat ventral posterolateral thalamus. J. Neurophysiol. 99, 2291–2304.
Goloshevsky, A.G., et al., 2011. Mapping cortical representations of the rodent forepaw and hindpaw with BOLD fMRI reveals two spatial boundaries. Neuroimage 57, 526–538.
Grandjean, J., et al., 2014. Optimization of anesthesia protocol for resting-state fMRI in mice based on differential effects of anesthetics on functional connectivity patterns. Neuroimage 102 Pt 2, 838–847.
Guillery, R.W., Harting, J.K., 2003. Structure and connections of the thalamic reticular nucleus: advancing views over half a century. J. Comp. Neurol. 463, 360–371.
Han, S., et al., 2019. Gradient-echo and spin-echo blood oxygenation level-dependent functional MRI at ultrahigh fields of 9.4 and 15.2 Tesla. Magn. Reson. Med. 81, 1237–1246.
Hayton, S.M., et al., 1999. Comparison of the effects of four anaesthetic agents on somatosensory evoked potentials in the rat. Lab. Anim. 33, 243–251.
Herkenham, M., 1980. Laminar organization of thalamic projections to the rat neocortex. Science 207, 532–535.
Hyder, F., et al., 1994. Dynamic magnetic resonance imaging of the rat brain during forepaw stimulation. J. Cereb. Blood Flow Metab. 14, 649–655.
Jones, E.G., 2012. The Thalamus. Springer Science & Business Media.
Jung, W.B., et al., 2016. Neuroplasticity for spontaneous functional recovery after neonatal hypoxic ischemic brain injury in rats observed by functional MRI and diffusion tensor imaging. Neuroimage 126, 140–150.
Keilholz, S.D., et al., 2004. Functional MRI of the rodent somatosensory pathway using multislice echo planar imaging. Magn. Reson. Med. 52, 89–99.
Kim, S.G., et al., 2013. Cerebral blood volume MRI with intravascular superparamagnetic iron oxide nanoparticles. NMR Biomed. 26, 949–962.
Kim, S.G., Ogawa, S., 2012. Biophysical and physiological origins of blood oxygenation level-dependent fMRI signals. J. Cereb. Blood Flow Metab. 32, 1188–1206.
Kim, T., et al., 2007. Arterial versus total blood volume changes during neural activity-induced cerebral blood flow change: implication for BOLD fMRI. J. Cereb. Blood Flow Metab. 27, 1235–1247.
Kim, T., et al., 2010. Frequency-dependent neural activity, CBF, and BOLD fMRI to somatosensory stimuli in isoflurane-anesthetized rats. Neuroimage 52, 224–233.
Komaki, Y., et al., 2016. Functional brain mapping using specific sensory-circuit stimulation and a theoretical graph network analysis in mice with neuropathic allodynia. Sci. Rep. 6, 37802.
Krause, M., et al., 2003. Auditory sensory gating in hippocampus and reticular thalamic neurons in anesthetized rats. Biol. Psychiatry 53, 244–253.
Kruger, G., Glover, G.H., 2001. Physiological noise in oxygenation-sensitive magnetic resonance imaging. Magn. Reson. Med. 46, 631–637.
Kruger, G., et al., 2001. Neuroimaging at 1.5 T and 3.0 T: comparison of oxygenation-sensitive magnetic resonance imaging. Magn. Reson. Med. 45, 595–604.
Lei, H., et al., 2001. The effects of ketamine-xylazine anesthesia on cerebral blood flow and oxygenation observed using nuclear magnetic resonance perfusion imaging and electron paramagnetic resonance oximetry. Brain Res. 913, 174–179.
Liao, C.C., et al., 2010. Distribution of large terminal inputs from the primary and secondary somatosensory cortices to the dorsal thalamus in the rodent. J. Comp. Neurol. 518, 2592–2611.
Liao, C.C., Yen, C.T., 2008. Functional connectivity of the secondary somatosensory cortex of the rat. Anat. Rec. 291, 960–973.
Lopez-Bendito, G., Molnar, Z., 2003. Thalamocortical development: how are we going to get there? Nat. Rev. Neurosci. 4, 276–289.
Maeng, S., et al., 2008. Cellular mechanisms underlying the antidepressant effects of ketamine: role of alpha-amino-3-hydroxy-5-methylisoxazole-4-propionic acid receptors. Biol. Psychiatry 63, 349–352.
Mandeville, J.B., et al., 1998. Dynamic functional imaging of relative cerebral blood volume during rat forepaw stimulation. Magn. Reson. Med. 39, 615–624.
Masliah, E., et al., 2000. Dopaminergic loss and inclusion body formation in alpha-synuclein mice: implications for neurodegenerative disorders. Science 287, 1265–1269.
Maxwell, C.R., et al., 2006. Ketamine produces lasting disruptions in encoding of sensory stimuli. J. Pharmacol. Exp. Ther. 316, 315–324.
Nair, G., Duong, T.Q., 2004. Echo-planar BOLD fMRI of mice on a narrow-bore 9.4 T magnet. Magn. Reson. Med. 52, 430–434.
Nasrallah, F.A., et al., 2014. Detection of functional connectivity in the resting mouse brain. Neuroimage 86, 417–424.
Nicolelis, M.A., Fanselow, E.E., 2002. Thalamocortical [correction of Thalamcortical] optimization of tactile processing according to behavioral state. Nat. Neurosci. 5, 517–523.
Oh, S.W., et al., 2014. A mesoscale connectome of the mouse brain. Nature 508, 207–214.
Olney, J.W., et al., 1999. NMDA receptor hypofunction model of schizophrenia. J. Psychiatr. Res. 33, 523–533.
Orser, B.A., et al., 1997. Multiple mechanisms of ketamine blockade of N-methyl-D-aspartate receptors. Anesthesiology 86, 903–917.
Paxinos, G., 2014. The Rat Nervous System. Academic press.
Pelled, G., et al., 2009. Ipsilateral cortical fMRI responses after peripheral nerve damage in rats reflect increased interneuron activity. Proc. Natl. Acad. Sci. U. S. A. 106, 14114–14119.
Petersen, C.C., 2014. Cortical control of whisker movement. Annu. Rev. Neurosci. 37, 183–203.
Petrinovic, M.M., et al., 2016. A novel anesthesia regime enables neurofunctional studies and imaging genetics across mouse strains. Sci. Rep. 6, 24523.
Pohmann, R., et al., 2016. Signal-to-noise ratio and MR tissue parameters in human brain imaging at 3, 7, and 9.4 tesla using current receive coil arrays. Magn. Reson. Med. 75, 801–809.
Power, J.D., et al., 2012. Spurious but systematic correlations in functional connectivity MRI networks arise from subject motion. Neuroimage 59, 2142–2154.
Prando, S., et al., 2019. Effects of ketamine/xylazine and isoflurane on rat brain glucose metabolism measured by (18) F-fluorodeoxyglucose-positron emission tomography. Eur. J. Neurosci. 49, 51–61.
Reimann, H.M., et al., 2018. Somatosensory BOLD fMRI reveals close link between salient blood pressure changes and the murine neuromatrix. Neuroimage 172, 562–574.

Schlegel, F., et al., 2015. The hemodynamic response to somatosensory stimulation in mice depends on the anesthetic used: implications on analysis of mouse fMRI data. Neuroimage 116, 40–49.
Schroeter, A., et al., 2017. Contributions of structural connectivity and cerebrovascular parameters to functional magnetic resonance imaging signals in mice at rest and during sensory paw stimulation. J. Cereb. Blood Flow Metab. 37, 2368–2382.
Schroeter, A., et al., 2014. Specificity of stimulus-evoked fMRI responses in the mouse: the influence of systemic physiological changes associated with innocuous stimulation under four different anesthetics. Neuroimage 94, 372–384.
Seamans, J., 2008. Losing inhibition with ketamine. Nat. Chem. Biol. 4, 91–93.
Seehafer, J.U., et al., 2010. No increase of the blood oxygenation level-dependent functional magnetic resonance imaging signal with higher field strength: implications for brain activation studies. J. Neurosci. 30, 5234–5241.
Sherman, S.M., 2016. Thalamus plays a central role in ongoing cortical functioning. Nat. Neurosci. 19, 533–541.
Shim, H.J., et al., 2018. Mouse fMRI under ketamine and xylazine anesthesia: robust contralateral somatosensory cortex activation in response to forepaw stimulation. Neuroimage 177, 30–44.
Silva, A.C., Koretsky, A.P., 2002. Laminar specificity of functional MRI onset times during somatosensory stimulation in rat. Proc. Natl. Acad. Sci. U. S. A. 99, 15182–15187.
Silva, A.C., et al., 1999. Simultaneous blood oxygenation level-dependent and cerebral blood flow functional magnetic resonance imaging during forepaw stimulation in the rat. J. Cereb. Blood Flow Metab. 19, 871–879.
Smith, S.M., et al., 2004. Advances in functional and structural MR image analysis and implementation as FSL. Neuroimage 23 (Suppl. 1), S208–S219.
Triantafyllou, C., et al., 2005. Comparison of physiological noise at 1.5 T, 3 T and 7 T and optimization of fMRI acquisition parameters. Neuroimage 26, 243–250.
Triantafyllou, C., et al., 2011. Physiological noise and signal-to-noise ratio in fMRI with multi-channel array coils. Neuroimage 55, 597–606.
Uludag, K., Blinder, P., 2018. Linking brain vascular physiology to hemodynamic response in ultra-high field MRI. Neuroimage 168, 279–295.
Vandamme, T.F., 2014. Use of rodents as models of human diseases. J. Pharm. BioAllied Sci. 6, 2–9.
Vollenweider, F.X., Kometer, M., 2010. The neurobiology of psychedelic drugs: implications for the treatment of mood disorders. Nat. Rev. Neurosci. 11, 642–651.
Wells, J.A., et al., 2017. Functional MRI of the reserpine-induced putative rat model of fibromyalgia reveals discriminatory patterns of functional augmentation to acute nociceptive stimuli. Sci. Rep. 7, 38325.
Williams, K.A., et al., 2010. Comparison of alpha-chloralose, medetomidine and isoflurane anesthesia for functional connectivity mapping in the rat. Magn. Reson. Imaging 28, 995–1003.
Wilson, C.J., 2014. The sensory striatum. Neuron 83, 999–1001.
Zakiewicz, I.M., et al., 2014. Brain-wide map of efferent projections from rat barrel cortex. Front. Neuroinf. 8, 5.
Zhao, F., et al., 2006. Cortical layer-dependent BOLD and CBV responses measured by spin-echo and gradient-echo fMRI: insights into hemodynamic regulation. Neuroimage 30, 1149–1160.
Zhao, F., et al., 2008. BOLD study of stimulation-induced neural activity and resting-state connectivity in medetomidine-sedated rat. Neuroimage 39, 248–260.